

**BLACK HOLE MASS OF ACTIVE GALACTIC NUCLEI
AT $z = 0.11 - 0.13$**

NATACHA UPRA

**A SENIOR PROJECT SUBMITTED IN
PARTIAL FULFILMENT
OF THE REQUIREMENTS FOR
THE DEGREE OF BACHELOR OF SCIENCE
(PHYSICS)
MAHIDOL UNIVERSITY INTERNATIONAL COLLEGE
MAHIDOL UNIVERSITY
2022**

COPYRIGHT OF MAHIDOL UNIVERSITY

Senior Project

entitled

BLACK HOLE MASS OF ACTIVE GALACTIC NUCLEI AT

$$z = 0.11 - 0.13$$

was submitted to the Mahidol University International College, Mahidol University
for the degree of Bachelor of Science (Physics)

on

08/04/2022

.....
Natacha Upa
Candidate

.....
Asst. Prof. Suraphong Yuma, D.Sc.
Advisor

.....
Asst. Prof. Aram Tangboonduangjit,
Ph.D
Chair of Science Division
Mahidol University International College
Mahidol University

.....
Weerapong Phadungsukanan, Ph.D.
Program Director
Bachelor of Science in Physics
Mahidol University International College
Mahidol University

ACKNOWLEDGEMENTS

I can't begin to describe how grateful I am for an opportunity to do this project, for everyone who helped me along the way, and for having the most awesome advisor yet. Aj. Suraphong Yuma, I would like to thank you for supervising my project, helping me in every way possible throughout my journey, and making my dream of always wanting to do astrophysics come true. This project got me through my best and my worse days, and I cannot be more proud of it.

I would also like to thank my two seniors, Kantapon Jensangjun and Chaipak Sawasdee, who helped me with the data source, the code, and giving me very much needed advice over the entirety of this project.

Aj. Teeraparb Chantavat, Aj. Tirawut Worrakitpoonpon, and everyone else in the CAEXAR group, I appreciate all your help and encouragement since day one until my last day of this project. It meant a great deal to me. In addition, Aj. Thaned Pruttivarasin, without whom, this project might not even happen. Thank you for your suggestions and advice you gave which brought me to where I am today.

Thank you Chakeera Wansoh and Tasfia Ahsan. Both of you were there with me throughout, and despite being annoyed by me so many times with my physics and my project, you were always around. I cannot express enough my gratitude to the two of you. You are a big part behind who I am and what I have achieved.

Mom, I can't thank you enough. You know I love physics and although you never understood what it was, you gave it your all for me. The past 5 years has been a blessing and it would not be possible without your constant support and always being by my side.

Last but not least, everyone in MUIC Physics major, including all the ajarns, friends, seniors and juniors. Thank you for always being there for me and always having my back, project-related or not. You guys have been amazing and I could not be happier having all of you in my life. And to the juniors specifically, if you are reading this, I would like you to use this project as a way to *not* do your own project. Do the complete opposite of what I did and your life will be full of glory :)

Natacha Upa

BLACK HOLE MASS OF ACTIVE GALACTIC NUCLEI AT $z = 0.11 - 0.13$.

NATACHA UPRA 6080507 ICPY/B

B.Sc. (PHYSICS)

SENIOR PROJECT ADVISORS : SURAPHONG YUMA, (PHYSICS)

ABSTRACT

The aim of this project is to calculate the black hole mass of 8 objects at $z > 0.112$, observed by Sloan Digital Sky Survey - IV (SDSS - IV) Mapping Nearby Galaxies at Apache Point Observatory (MaNGA). Using the flux density spectrum, the flux of the $[\text{OIII}]\lambda 5007\text{\AA}$ emission line is computed, and with that, its luminosity. The M_{BH} is obtained using the luminosity of the same emission line, which is converted to the bolometric luminosity using the relation $L_{\text{Bol}} = 3200L_{[\text{OIII}]}$ (Shen et al., 2011), and a relationship presented by Ferris et al. (2021).

The correlation between M_{BH} and velocity dispersion is also analyzed. There is a weak relationship found between M_{BH} and σ , for both σ_* and $\sigma_{\text{H}\alpha}$. However, the results acquired in this work is, to a great extent, an underestimate compared to the results in other studies, where the correlation is seen to be much stronger.

KEY WORDS : BLACK HOLES; BLACK HOLE MASS; ACTIVE GALACTIC NUCLEI; FLUX; LUMINOSITY; VELOCITY DISPERSION

30 pages

CONTENTS

| | |
|--|------------|
| ACKNOWLEDGEMENTS | iii |
| ABSTRACT (ENGLISH) | iv |
| 1 Introduction | 1 |
| 2 Literature Review | 3 |
| 2.1 Active Galactic Nuclei | 3 |
| 2.1.1 The Unified Model of AGN | 3 |
| 2.2 Supermassive Black Holes | 4 |
| 2.2.1 Reverberation Mapping | 5 |
| 2.2.2 M_{BH} - σ relation | 6 |
| 2.2.3 M_{BH} - Luminosity relation | 7 |
| 3 Sample | 8 |
| 3.1 MaNGA | 8 |
| 3.2 Sample Selection Criteria | 8 |
| 3.3 Sample list | 9 |
| 3.4 Structure of the Object's Data | 9 |
| 4 Methods | 12 |
| 4.1 Flux Density | 12 |
| 4.2 Checking the Existence of [OIII] Emission Line | 12 |
| 4.3 Filtering the Background Noise | 13 |
| 4.4 Flux | 14 |
| 4.4.1 Selecting Region | 15 |
| 4.4.2 Intersection Point | 15 |
| 4.4.3 Straight Line | 16 |
| 4.4.4 Wavelength Value of the Intersection | 17 |
| 4.4.5 Area Under the Peak | 17 |
| 4.4.6 Continuum | 18 |
| 4.5 Luminosity | 19 |
| 4.5.1 Luminosity Distance | 19 |
| 4.6 Error Analysis | 20 |
| 5 Results | 21 |
| 5.1 Flux and Luminosity | 21 |
| 5.2 Velocity Dispersion | 21 |

CONTENTS (CONT.)

vi

| | |
|---------------------|-----------|
| 6 Discussion | 25 |
| 7 Conclusion | 27 |
| REFERENCES | 28 |
| BIOGRAPHY | 30 |

CHAPTER 1

INTRODUCTION

Active galaxies, unlike any other ordinary galaxies, contains an active supermassive black hole at the core that feeds on the accretion disk surrounding it. Infalling matter from the accretion disk into the black hole is the main engine that drive the active galaxies, which could result in them having a full range electromagnetic radiation emission and explains their large energy output. This shows that the core of the active galaxies, or the active galactic nuclei (AGN), are dependent on the accretion of the central black hole, and thus, knowing information about said black hole would make it possible to infer it to the host galaxies.

One way the properties of AGNs can be determined is through the use of M_{BH} of the central black hole. There has been many attempts to find the M_{BH} . One very solid method is reverberation mapping, which uses the time taken for the variation in the inner, continuum region of the AGN to cause visible changes in the outer, broad line region to find the size of the AGN, and hence the mass of the black hole. Another method is based on the $M_{\text{BH}} - \sigma$ relation, which uses the stellar velocity dispersion to calculate the mass of black holes and consequently, its correlation to the host galaxy. The method employed in this report, however, uses the luminosity of an [OIII] emission line, along with a relationship found from a previous study to calculate M_{BH} . This method calculates the [OIII] flux, and from that, its luminosity, and with the luminosity known, the M_{BH} can be calculated. The choice of [OIII] was made because of its high ionization energy which implies that the source has to be an AGN or a black hole as stars in general do not have sufficient energy to produce such emission.

This work uses data from Sloan Digital Sky Survey (SDSS) Mapping Nearby Galaxies at Apache Point Observatory (MaNGA), which stores sky subtracted, calibrated

information on observed objects as a 3-dimensional data cube, thus making it possible to perform calculations on both spatial and spectral dimensions. MaNGA data are used here to produce the flux density spectrum of 8 individual objects. [OIII] flux and luminosity are then obtained from the spectrum and subsequently, the M_{BH} from the luminosity. The M_{BH} of the 8 objects will then be used to examine the $M_{\text{BH}} - \sigma$ relation, in comparison with previous studies.

CHAPTER 2

LITERATURE REVIEW

2.1 Active Galactic Nuclei

Nestling at the heart of galaxies, is a dense and compact region called Active Galactic Nuclei, or AGN. They are responsible for explaining a fraction of galaxies in which their nuclei, despite being extremely small in size, are observed to have luminosity higher than its host galaxy (Mo et al., 2010), and displays non-stellar emission (Romero & Vila, 2014), as opposes to normal stellar spectrum which contains mostly absorption lines (Mo et al., 2010). AGNs have a broad electromagnetic radiation spectrum, ranging from radio waves to X-ray, or even gamma rays (Schneider, 2014).

Employing a method to categorize AGNs using their properties, such as their emission line spectra, their polarization properties, and the shape of their host galaxy, makes it possible to classify AGNs into many different classes. These classes include Seyferts, Quasars, Radio Galaxies, Blazars, ULIRGs (Ultra Luminous Infrared Galaxies), and LINERs (Low Ionization Nuclear Emission-lines Regions) (Carroll & Ostlie, 2017). Physical activities of AGNs which leads to the generation of X-ray, ultraviolet, and radio electromagnetic radiation suggest the existence of an active supermassive black holes with mass ranging from $10^6 M_{\odot} - 10^9 M_{\odot}$ within them (Frolov & Zelnikov, 2011).

2.1.1 The Unified Model of AGN

Observations have shown that, although the different types of AGN displays different properties, there are certain characteristics which are shared across all classes of AGN. For that, questions began to arise to whether or not all AGNs are intrinsically the same but only appear different because of the difference in their orientations when being viewed.

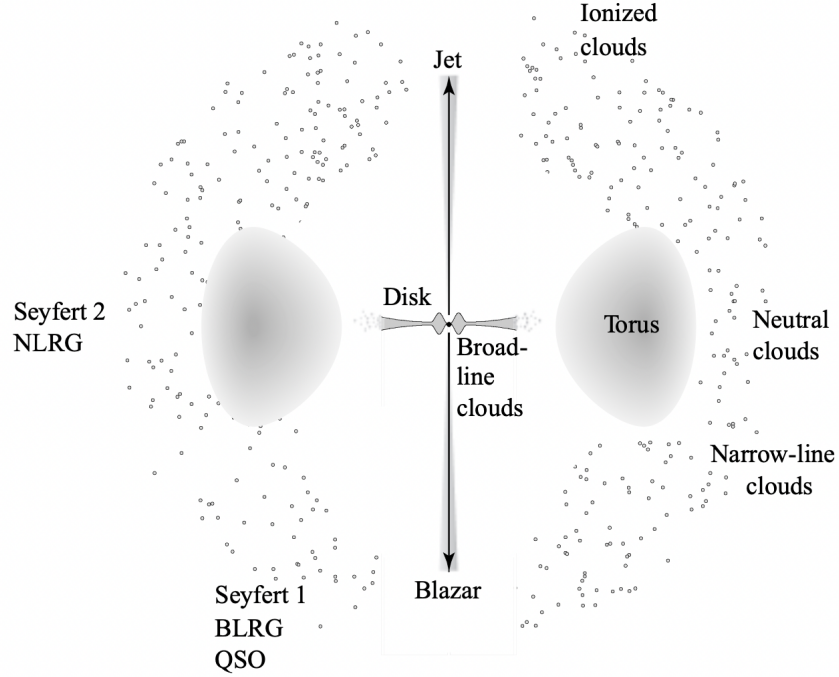


Figure 2.1: Structure of a unified model of AGN (Carroll and Ostlie, 2017)

Figure 2.1 shows an image of a unified model of AGN. The image shows the structure of the AGN, where the central, rotating, supermassive black hole is surrounded by the accretion disk, which is the central engine of the AGN, and the broad line region, or BLR. Ejecting out from the center is the jet of charged particles and encircling that is the dusty torus and the narrow line region, or NLR. The type of AGN that would be observed at different viewing angles is also presented (Carroll and Ostlie, 2017).

2.2 Supermassive Black Holes

Supermassive black holes (SMBH) are black holes which are defined to have mass ranging from, approximately, $10^6 M_{\odot} - 10^{10} M_{\odot}$. They are known to exist at the core of most galaxies, including our very own Milky Way galaxy, which holds a SMBH with the mass of roughly $4 \times 10^6 M_{\odot}$ (Romero & Vila, 2014).

Experiments have been carried out in the past, with numerous attempts adopting various methods to find the mass of SMBHs. These techniques include reverberation mapping, which finds the mass of SMBHs using changes in the BLR of the AGN, M_{BH}

- σ relation, which uses the fact that there is a link between M_{BH} and the velocity dispersion, σ , of the galaxy, and the relationship of M_{BH} with its luminosity, which is based on observations that there is a correlation between luminosity and M_{BH} .

2.2.1 Reverberation Mapping

Responsible for the majority of the gravitational force of the galaxy is a SMBH living at its center. The SMBH is surrounded by an accretion disk, made of gas and dust. Continuum emission of AGN is caused by the infalling of matter into the SMBH, which then heats the accretion disk via viscous heating (Peterson, 1993). The BLR, surrounds the accretion disk, as shown in figure 2.1.

Reverberation mapping technique uses the fact that heating and ionization in the continuum region of the accretion disk causes a physical and detectable changes in the BLR. Observations show that there is a rapid variation in the BLR which leads to a conclusion that either the continuum source is very small, or the BLR must be close to the central region (Peterson, 1993).

The time taken for changes in the continuum region to reach the BLR, resulting in visible emission lines, is

$$\Delta t \sim \frac{r}{c} \quad (2.1)$$

where

r is the size of the BLR; and

c is the speed of light.

Note that since the observers are not observing at a position which is equidistant from all points of the BLR, they will see a delayed response in the observable region. It would be helpful to consider the point in which the observers would detect changes after some time delay τ (Peterson, 1993).

From equation 2.1, the size r of the BLR can be determined, and with that, the M_{BH} can be found using (Schneider, 2014)

$$M_{\text{BH}} = \frac{f r \sigma^2}{G} \quad (2.2)$$

where

f is a factor that depends on the geometry and kinematics of the BLR. The more accurately determined the factor f , the more precise the value of the M_{BH} . $f \sim 1$ for circular orbits (Schneider, 2014);

σ is the velocity dispersion; and

G is the gravitational constant.

Although very reliable, reverberation mapping is a painfully slow process as it requires continuous observation of the continuum source over a period of months, or even years.

2.2.2 M_{BH} - σ relation

Given the downside of reverberation mapping, it is crucial to find an alternative and dependable method, which calls for less amount of time. This substitute approach should give consistent results with previously calculated values. One such method is the M_{BH} - σ relations, where σ is the velocity dispersion.

Ferrarese and Merritt (2000), and Nelson et al. (2004) derived a correlation between M_{BH} and the velocity dispersion of the host galaxy, with $M_{\text{BH}} \propto \sigma^\alpha$. $\alpha = 4.8 \pm 0.5$ was founded by Ferrarese and Merritt (2000), while Nelson et al. obtained $\alpha = 4.1 \pm 0.5$.

Gebhardt et al. (2000), Sparke and Gallagher (2007), Mo et al. (2010), McConnell and Ma (2013), Schneider (2014), and Carroll and Ostlie (2017) established a more concrete relationship between M_{BH} and the stellar velocity dispersion, σ_* , as follow

$$M_{\text{BH}} = \alpha \times 10^8 M_\odot \left(\frac{\sigma_*}{200 \text{ km s}^{-1}} \right)^\gamma \quad (2.3)$$

where α ranges from 1.2 ± 0.2 to $2.14^{+0.26}_{-0.23}$ and γ is bounded within 3.75 ± 0.3 and 5.57 ± 0.33 .

Unfortunately, this method can only be used with a limited number of AGNs, since they can either be too distant, or too luminous, to which their velocity dispersion cannot be accurately measured.

2.2.3 M_{BH} - Luminosity relation

This report uses another possible way to find the M_{BH} using [OIII] λ 5007 emission line as a proxy for the bolometric luminosity. The choice of [OIII] was made because the ionisation energy of [OIII] is much higher (about 35eV) compared to that of [OII] (about 13eV), which would correspond to light in the far UV and X-ray region. Stars, in general, are incapable of producing such wavelengths, so the chosen objects with [OIII] luminosity must be supermassive stars, or AGN with a black hole.

Also, the production of [OIII] line in an AGN is caused by ionising radiation in the NLR which is outside the obscuring regions of the AGN, thus the [OIII] emission line will be less attenuated compared to other emission lines from the inner regions. (Heckman & Best, 2014)

Using a bolometric conversion factor $L_{\text{bol}} = 3200L_{[\text{OIII}]}$ (Shen et al., 2011), Ferris et al. (2021) derived, using the comparisons of spectral properties of broad line quasars from SDSS DR7, a correlation between M_{BH} and $L_{[\text{OIII}]}$ to be

$$\frac{M_{\text{BH}}}{M_{\odot}} = \frac{3200 \times L_{[\text{OIII}]}}{\lambda_{\text{Edd}} \times 3.28 \times 10^4} \quad (2.4)$$

where

M_{BH} is the black hole mass;

M_{\odot} is the solar mass, which is equal to 2×10^{30} kg;

λ_{Edd} is the Eddington ratio; and

$L_{[\text{OIII}]}$ is the luminosity of the [OIII] emission line, in solar luminosity, L_{\odot} , where $L_{\odot} = 3.846 \times 10^{33}$ erg s⁻¹.

The value of λ_{Edd} is chosen to be 1 to produce the lower limit on the M_{BH} , assuming that the source is in hydrostatic equilibrium (Ferris et al., 2021).

CHAPTER 3

SAMPLE

3.1 MaNGA

MaNGA is a two-dimensional spectroscopic survey that uses integral field unit (IFU) spectroscopy to measure spectra for each galaxy in the 3,622 - 10,354 Å wavelength range (Law et al., 2016). MaNGA uses fiber-bundles IFU, arranged into a hexagon, that has a diameter ranging from 12 to 32 arcsec, which corresponds to 19 fibers to 127 fibers, respectively (Bundy et al., 2014).

The MaNGA Data Reduction Pipeline (DRP) produces a flux calibrated and sky subtracted data for each galaxy from its raw data. Multiple flux calibrated exposures are combined into a three-dimensional data cube which is then feed into the Data Analysis Pipeline (DAP), where it produces the physical properties such as stellar kinematics, velocity maps, and emission line properties for 21 different emission lines (Law et al., 2016; Wylezalek et al., 2020).

3.2 Sample Selection Criteria

The objects used in this paper were taken from the catalog of Wylezalek et al. (2020), which is based on SDSS - DR14. The sample set is then filtered and only objects with $z > 0.112$ are chosen, which are those with the [OIII] emission line falling in the R-band. There are 8 objects used in this work, of which its data are taken from SDSS - DR16, a fourth data release of SDSS - IV.

3.3 Sample list

Table 3.1: Table showing all the objects used. Each object is identified using their MaNGA ID. Their redshift value, z , RA, and Dec values are also given. This table is ordered according to the redshift value, from lowest to highest.

| MaNGA ID | z | RA (deg) | Dec. (deg) |
|----------|--------|-------------|------------|
| 1-156039 | 0.1147 | 143.9406592 | 49.0232114 |
| 1-43214 | 0.1180 | 114.0963833 | 39.4382798 |
| 1-22948 | 0.1194 | 254.5420840 | 62.4156480 |
| 1-258599 | 0.1256 | 186.1809966 | 44.4107712 |
| 1-72322 | 0.1262 | 121.0142005 | 40.8026130 |
| 1-284293 | 0.1291 | 197.2393190 | 45.9054470 |
| 1-269632 | 0.1315 | 247.5609730 | 26.2064736 |
| 1-574402 | 0.1320 | 115.3687198 | 44.4087940 |

3.4 Structure of the Object's Data

For demonstration purposes, the figures in this report will be taken from an object with MaNGA ID 1-43214, which is one of the objects in the sample list in table 3.1. This object is not in any way more significant than the others.

The data of the objects were in the format of a FITS (Flexible Image Transport System) file, which is the most common file type used in astronomy to store images and tables. The important data sets within each FITS file of each objects that were used are : FLUX, IVAR, MASK, and WAVE, where FLUX gives the value of flux density and IVAR gives the values of the corresponding inverse variance. The MASK gives the criteria to determine whether or not each flux density value for a certain spaxel is to be masked, and the WAVE contains the observed wavelengths.

The FLUX, IVAR, and MASK data are given as a 3-dimensional array, with the dimension of $(n, n, 4563)$, where n is the number of pixels of the length and width of the

image of the object observed, and 4,563 is the number of wavelengths that were observed in each object. Each of the three data sets contains $n \times n \times 4563$ spaxels, and each value in the array corresponds to a specific spaxel. The WAVE data, on the other hand, is given as a 1-dimensional array, containing all the 4,563 the wavelength values that were used in the observation.

The wavelengths that were observed are from 3,622Å to 10,354 Å, spaced unevenly, with an increasing difference between each value, into 4,563 wavelength points. The observed wavelengths used are the same for every objects.

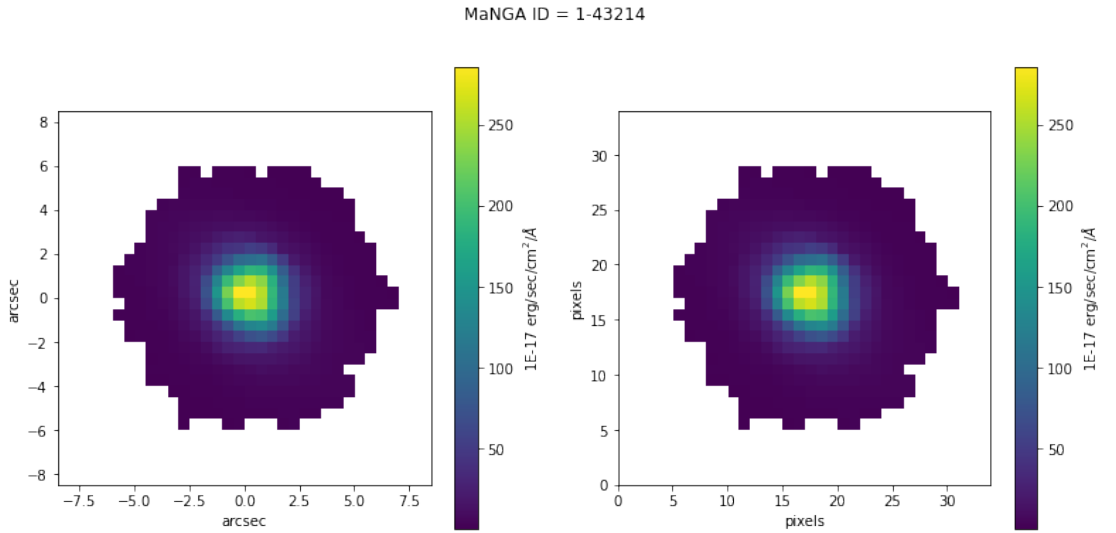


Figure 3.1: Example of a 2-dimensional image, constructed from a 3-dimensional data, showing the flux density values of the object with MaNGA ID 1-43214, which has a dimension of (34, 34, 4563). Flux density values are taken at wavelengths 5,575 - 5,625 Å, and are then summed. The axes of the figure on the left shows the angle subtended by the object in the sky, given in arcsec, and the axes of the figure on the right shows the number of pixels covered by the object.

Flux density spectrum is also another way to display the information about the object. It can be represented by a graph showing the summation of all the flux density values of every spaxels at each wavelength in the desired range. Figure 3.2 shows the central spectrum of flux density of object 1-43214, that is, it shows the flux density of only the central spaxel, at all observed wavelength. This is to ensure that the flux density at every wavelength will be covered and there would be minimal noise, as the noise tends to increase and the flux density tends to decrease moving away from the

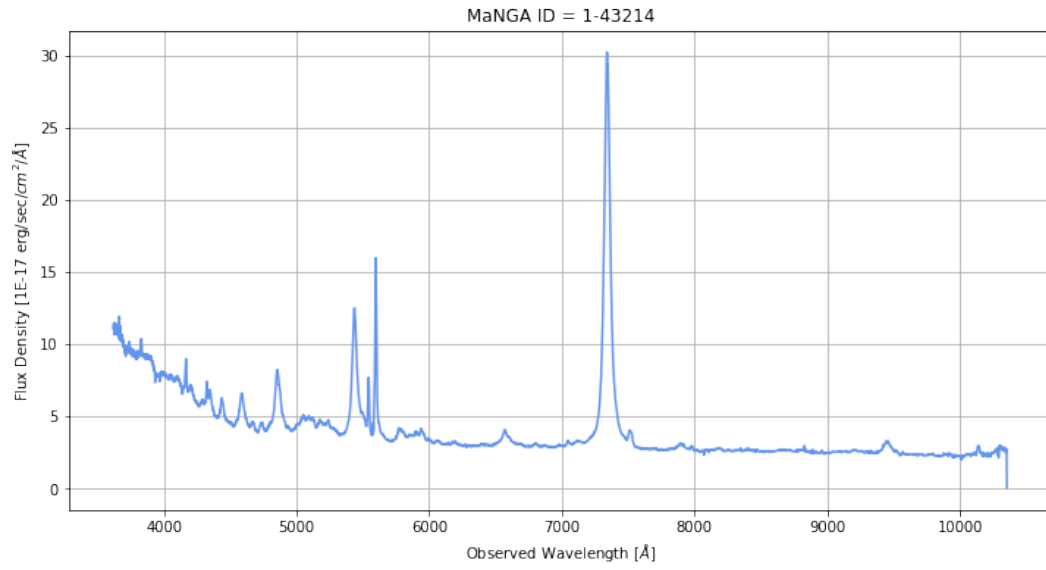


Figure 3.2: The central spectrum of the object with MaNGA ID 1-43214.

center of the object. The flux will be zero at the corner of the cubed data, as the IFU field is a hexagon.

CHAPTER 4

METHODS

4.1 Flux Density

Figure 4.1 shows the flux density spectrum of the object with MaNGA ID 1-43214. The values of the flux density per spaxel, from the FLUX data set, are masked according to the masking criteria given in the MASK data set. This will help get rid of the bad spaxels. The masked flux density values are then summed, at each of the 4,563 wavelengths, to produce the spectrum as shown.

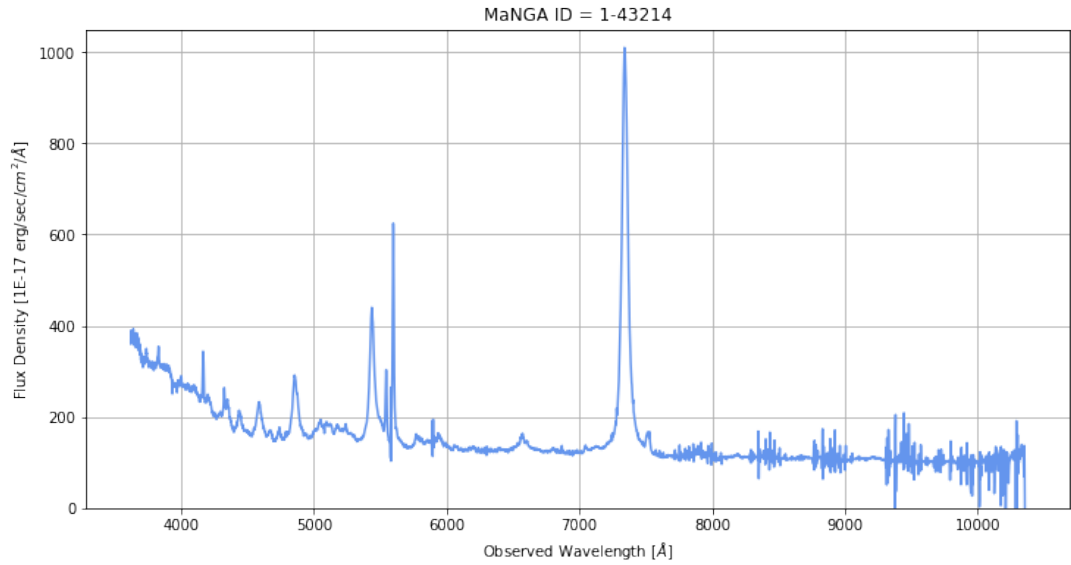


Figure 4.1: The flux density of the object with MaNGA ID 1-43214, given per wavelength in the observed frame.

4.2 Checking the Existence of [OIII] Emission Line

Prior to performing any calculations, it is pivotal to ensure that there exist an [OIII] emission line. Using the redshift, z , of the object and the rest frame wavelength, λ_{rest} of [OIII], which is 5007 Å, the observed wavelength, λ_{obs} , can be determined by

$$1 + z = \frac{\lambda_{\text{obs}}}{\lambda_{\text{rest}}} \quad (4.1)$$

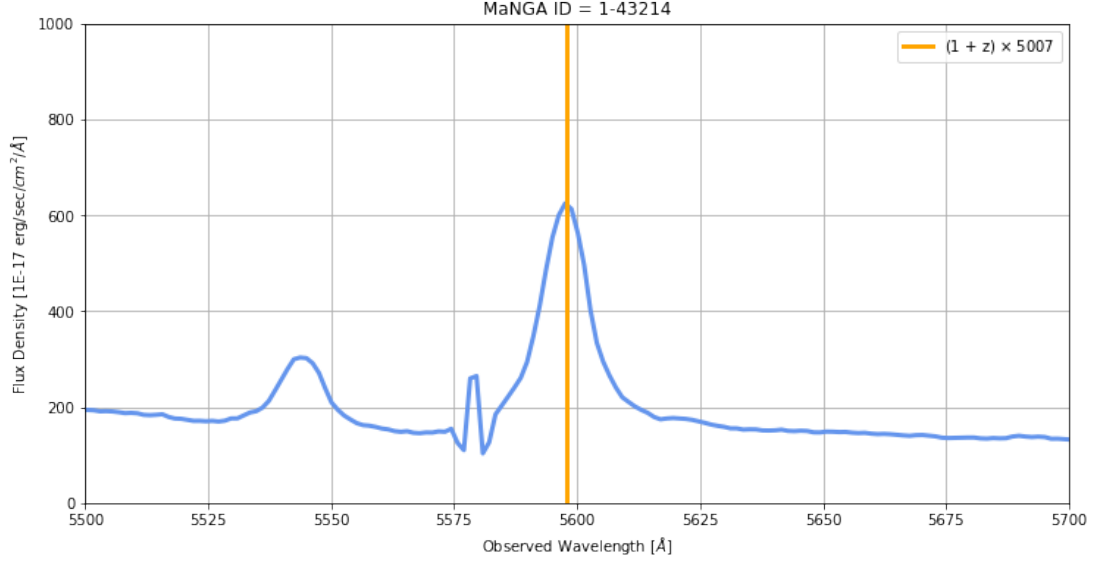


Figure 4.2: The orange line marking the value of observe wavelength, calculated from equation 4.1

In figure 4.2, the orange line marks the value of the observed wavelength, which was calculated using the redshift value of the object, and equation 4.1. With the orange line aligning with a peak, this shows that there exists an [OIII] emission line, and further calculations can be done using this specific peak.

4.3 Filtering the Background Noise

The values of the flux density given from the FLUX data file, although masked, still contains the unwanted flux density values of the background sky, which has to be filtered away to ensure that there will be no contamination. This can be done with the use of the inverse variance values given as IVAR in the data file.

The inverse variance values of the flux density are converted into the standard deviation values, σ , and flux density values in the observe frame which are below 3σ are filtered out.

Figure 4.3 shows the flux density spectrum before and after subtracting the noise. The dark blue line shows the spectrum before the subtraction and the light blue line shows the spectrum after subtraction. It can be seen that both the lines are almost perfectly superimposed showing that there are minimal background noise for this object.

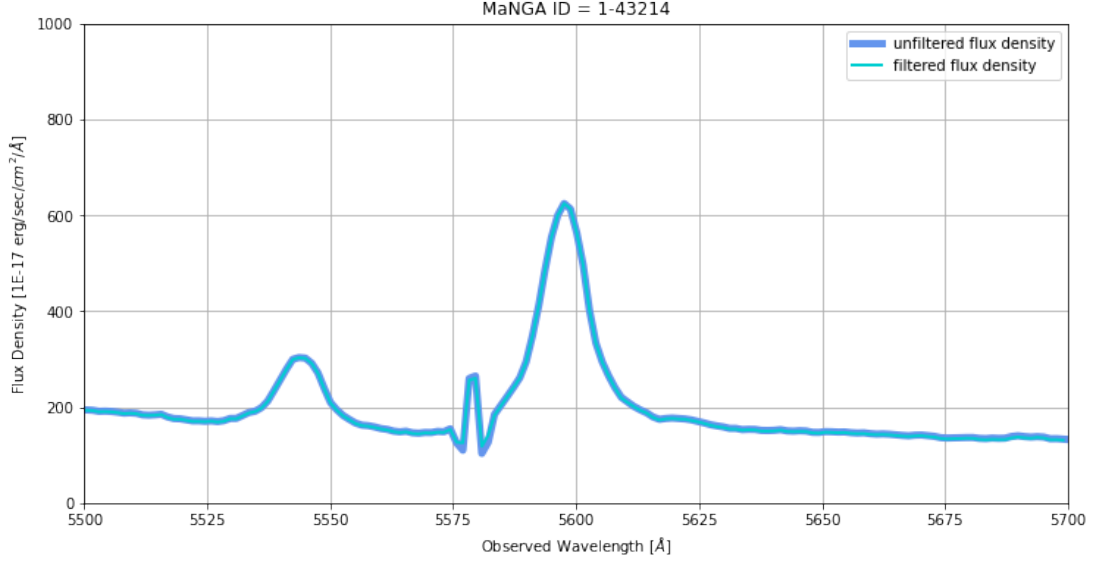


Figure 4.3: Flux density spectrum before and after filtering out the noise using the inverse variance.

4.4 Flux

After the peak of interest has been determined and cleaned of the noise, the flux will be calculated using it.

The flux, F , is defined as

$$F = \int_{\lambda_1}^{\lambda_2} f_{\lambda} d\lambda \quad (4.2)$$

where

f_{λ} is the flux density at each wavelength; and

λ_1 and λ_2 are the initial and final wavelengths of the peak of the emission line from the graph.

In other words, flux is defined as being the area under the graph within the region of the peak of interest. The following will give a walk-through on how the area under the peak was calculated.

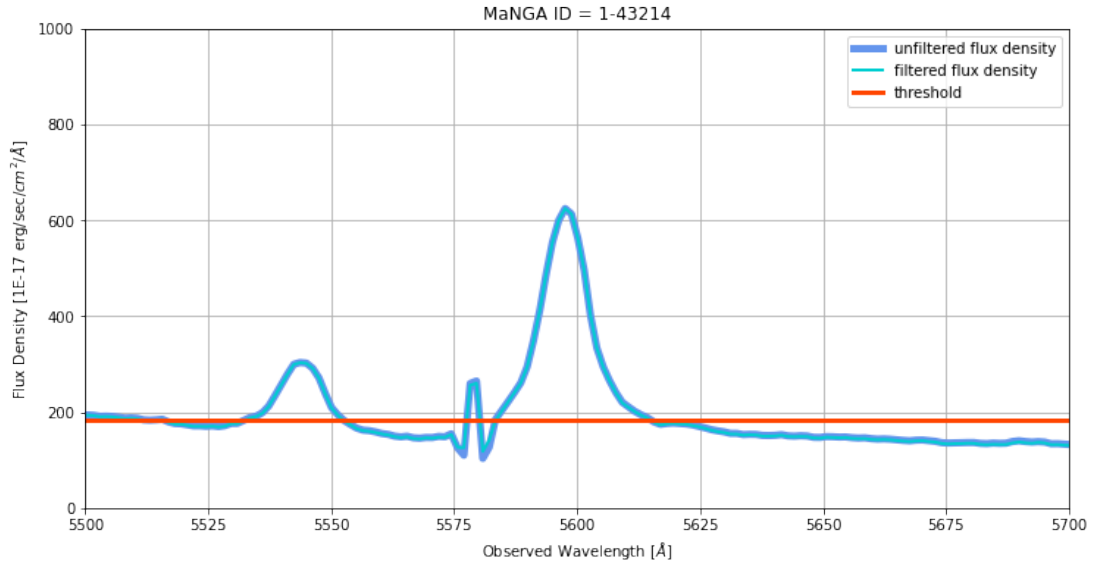


Figure 4.4: Graph showing the spectrum of both filtered and unfiltered flux density, and the threshold line.

4.4.1 Selecting Region

First, the threshold line needs to be marked, giving 2 intersection points, one on the left and the other on the right of the peak, as shown in figure 4.4. The value of the threshold line is chosen from the flux density data point on the spectrum which is at the base of the peak. In the case shown in figure 4.4, the height of the threshold line is equal to the flux density value on the left base of the peak.

Unfortunately, there does not exist a data point with the same flux density value at the other intersection, which in this case is the one on the right base of the peak, so an estimation will need to be made.

This will bound the peak to within the region between the two intersection points only.

4.4.2 Intersection Point

Figure 4.5 shows figure 4.4 but zoomed into the intersection on the right of the peak. The two pink markings show the data points obtained from the file, while the light blue line gives the estimate of the values in between each data point. It can be seen that the intersection between the flux density and the threshold line does not lie on any data

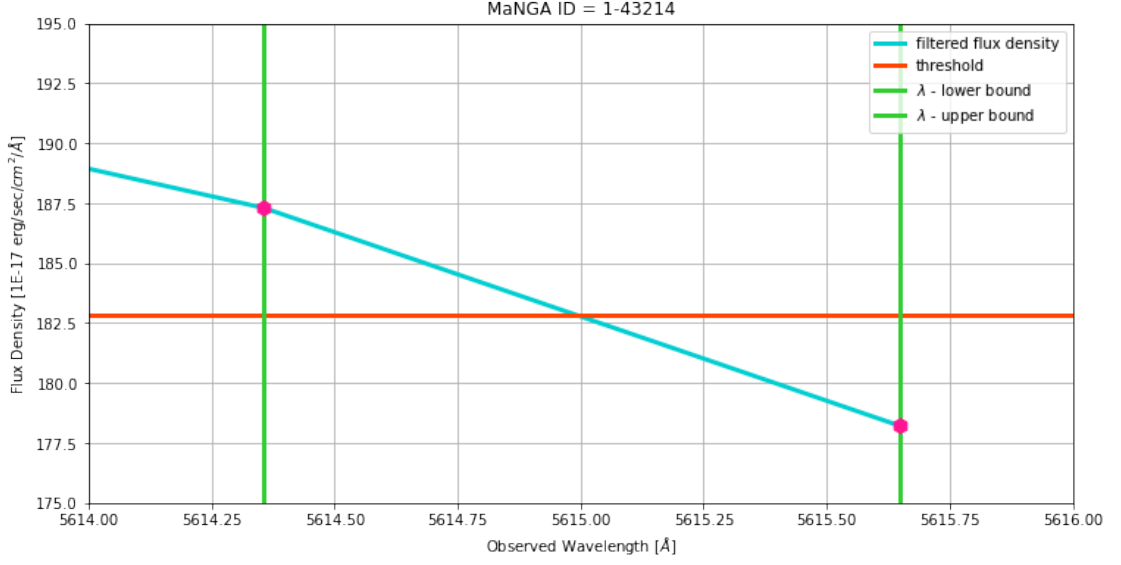


Figure 4.5: Intersection of the flux density and the threshold line. Pink plots show the data points and the green lines mark the wavelength at said data points, which also acts as the lower and upper bounds for the intersection calculations.

point.

In order to avoid the flux density below the threshold line, as it would exceed the region bounded earlier, the wavelength value of the intersection point needs to be determined. Selecting the data point that immediately precedes and immediately follows the intersection allows the flux density in between these two data points to be treated as a straight line.

4.4.3 Straight Line

To find the value of any point on a straight line, the equation of the line must be known. The equation of a straight line is in the form

$$y = mx + c \quad (4.3)$$

The gradient, m , is found using the coordinates of the two pink data points in the figure 4.5, as the following

$$m = \frac{f_{\lambda, \text{left}} - f_{\lambda, \text{right}}}{\lambda_{\text{left}} - \lambda_{\text{right}}} \quad (4.4)$$

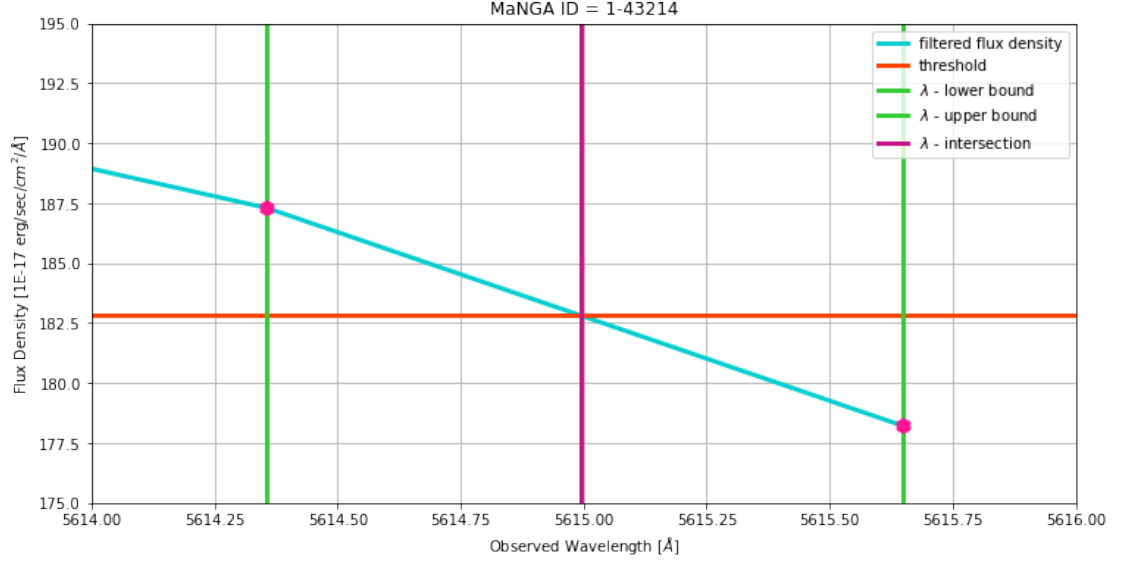


Figure 4.6: Magenta line marked at the wavelength value of the point of intersection.

where f_λ is the flux density value, and λ is the wavelength value of each of the two pink plots. Left and right indicates the position of the data points in figure 4.5 relative to one another.

After the value of the gradient is found, one the the two data point is chosen and is used to find the value of the y -intercept, c .

4.4.4 Wavelength Value of the Intersection

After the equation of the line is found, the value of the threshold is used as the value of y to find the corresponding value of x , which is the wavelength of the point of intersection. When found, it will look like figure 4.6, where the magenta line is marked at the wavelength value of the intersection point.

With the coordinates of the intersection point known, the [OIII] peak region of the flux density graph can be limited to above the threshold line, and only the data points on or above the line will be used to calculate the flux.

4.4.5 Area Under the Peak

Each pink data point in figure 4.7 gives the value of wavelength, and the corresponding flux density. From equation 4.2, flux is found by the sum of all $f_\lambda d\lambda$ at every

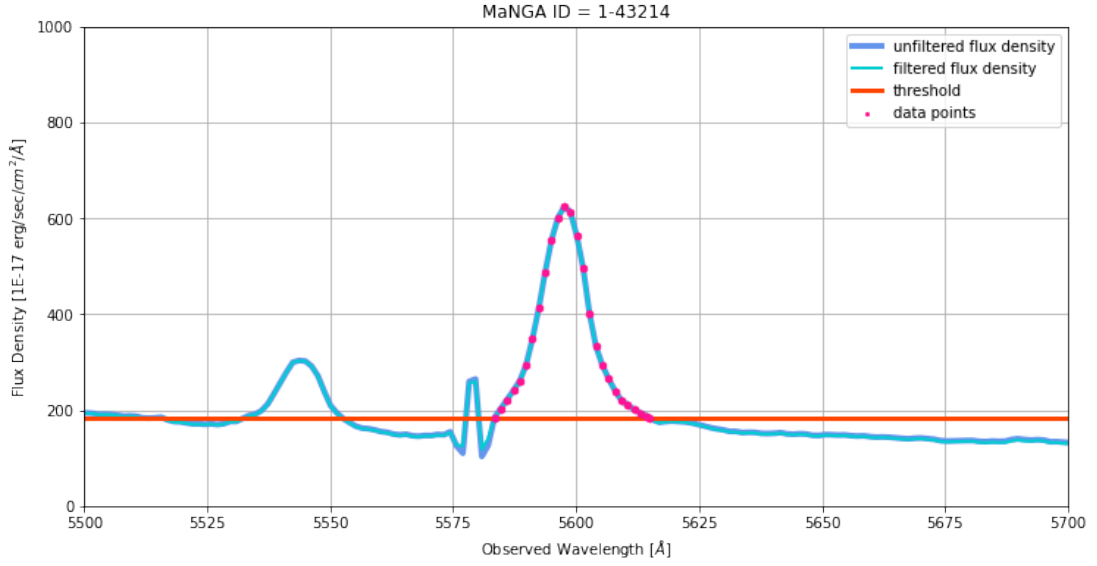


Figure 4.7: Figure showing data points on and above the threshold line.

data points within a selected region. The value of $d\lambda$ is the difference in wavelength values of two successive data points. Knowing f_λ and $d\lambda$, the area under the selected region, i.e., the flux, can be found using trapezium rule.

$$F = \frac{1}{2} \left(f_{\lambda,1} d\lambda_1 + f_{\lambda,2} (d\lambda_1 + d\lambda_2) + f_{\lambda,3} (d\lambda_2 + d\lambda_3) + \dots + f_{\lambda,n-1} (d\lambda_{n-2} + d\lambda_{n-1}) + f_{\lambda,n} d\lambda_{n-1} \right) \quad (4.5)$$

4.4.6 Continuum

The flux value calculated using equation 4.5 is the area of the region under the selected peak, bounded by the two intersections mentioned earlier, which consists of the area above the threshold line, and the area below the threshold line. The area below the threshold line is the continuum region, which should be subtracted from the total area to get the area of the peak above the threshold line only.

To find the area of the rectangle under the peak below the threshold line, the first and the last data point shown in pink in figure 4.7 are used. The width of the area is the difference between the wavelength values of the first and the last data points, and

the height of the area is equal to the threshold value. With that, the area can be found by multiplying the width and the height. This area is then subtracted from the total area, which would result in the flux of the [OIII] emission line.

4.5 Luminosity

With the value of the flux, i.e., the area under the peak above the threshold line, computed, the luminosity, in the unit of erg s^{-1} , can be calculated using

$$L = 4\pi d^2 F \quad (4.6)$$

where

d is the luminosity distance; and

F is the flux.

4.5.1 Luminosity Distance

The luminosity distance, D_L , is calculated using the help of a cosmology calculator made by Edward L. Wright (Wright, 2006), which take in parameters, including Hubble constant, H_0 , the density parameter for matter, Ω_M , the density parameter for dark energy, Ω_Λ , and the redshift, z , of the object. The values of H_0 , Ω_M , and Ω_Λ are constant, while the value of z depends on the object.

Assuming flat universe, as the area of observation is small enough that the effect of curvature is negligible, the values of each parameter are as follow

$$H_0 = 70 \text{ km/s/Mpc}$$

$$\Omega_M = 0.3$$

$$\Omega_\Lambda = 0.7$$

The luminosity distance obtained from the calculator is given in Mpc, while the unit of flux density is in the unit of cm , so the luminosity distance value has to be converted into cm by multiplying with a factor of 3.08568×10^{24} .

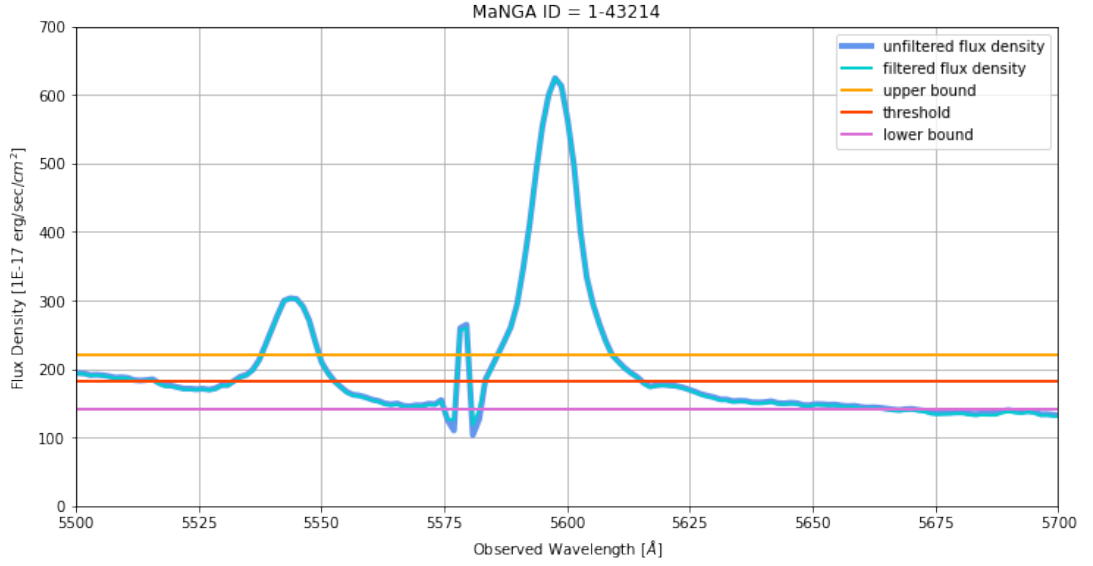


Figure 4.8: Flux density spectrum with threshold line and its upper bound and lower bound.

With D_L in the correct unit, and the value of flux found from the graph, the luminosity can be calculated using equation 4.6.

The luminosity of the [OIII] emission line, after dividing by L_\odot to obtain $L_{[\text{OIII}]}$ in solar luminosity, can be used to work out M_{BH} , in solar masses, by using equation 2.4.

4.6 Error Analysis

The values for flux, luminosity, and M_{BH} calculated earlier was not accounted for the possible errors. Since the starting point and ending point of the emission line peak is not well defined, it is likely that the choice of the threshold line would give rise to uncertainties, hence, the errors for said data will be calculated using the upper and lower bounds of the threshold value.

Figure 4.8 shows the threshold line (in red) and the upper and lower bound lines used to find the error in the value of flux. The method for error calculation is similar to that of the flux calculation. The uncertainty values calculated includes the uncertainty for flux, and from that, the uncertainty for luminosity and M_{BH} / subsequently.

CHAPTER 5

RESULTS

Table 5.1 shows the values of flux, along with its uncertainties, achieved from calculations. The luminosity distance is calculated using z , and with that, the values of $\log\left(\frac{L_{[\text{OIII}]}}{L_{\odot}}\right)$ and $\log\left(\frac{M_{\text{BH}}}{M_{\odot}}\right)$ are calculated.

5.1 Flux and Luminosity

Figure 5.1 (left) shows the value of [OIII] flux computed in this work against the value of [OIII] flux given in the catalog for each of the objects in the sample list, and (right) the value of $\log\left(\frac{L_{[\text{OIII}]}}{L_{\odot}}\right)$ in this work versus $\log\left(\frac{L_{[\text{OIII}]}}{L_{\odot}}\right)$ from the catalog. Both sets of values are presented along with their uncertainties.

5.2 Velocity Dispersion

The blue data points in figure 5.2 shows $\log\left(\frac{\sigma_{*}}{200 \text{ kms}^{-1}}\right)$ (on the bottom axis) and the pink data points shows $\log\left(\frac{\sigma_{\text{H}\alpha}}{200 \text{ kms}^{-1}}\right)$ (on the top axis). Both data sets are plotted against $\log\left(\frac{M_{\text{BH}}}{M_{\odot}}\right)$. The blue line shows the best fit line for the stellar velocity dispersion data, while the pink line shows the best fit line for the H α velocity dispersion. The green solid line is the line showing the relationship between M_{BH} and σ_{*} taken from Carroll and Ostlie (2017), where the dashed lines are the lower and the upper bounds of said relationship. The correlation is given as

$$M_{\text{BH}} = (1.66 \pm 0.24 \times 10^8) M_{\odot} \left[\frac{\sigma_{*}}{200 \text{ kms}^{-1}} \right]^{4.86 \pm 0.43} \quad (5.1)$$

A similar correlation for stellar velocity dispersion in this work is

$$M_{\text{BH}} = (9.75 \times 10^6) M_{\odot} \left[\frac{\sigma_{*}}{200 \text{ kms}^{-1}} \right]^{0.85} \quad (5.2)$$

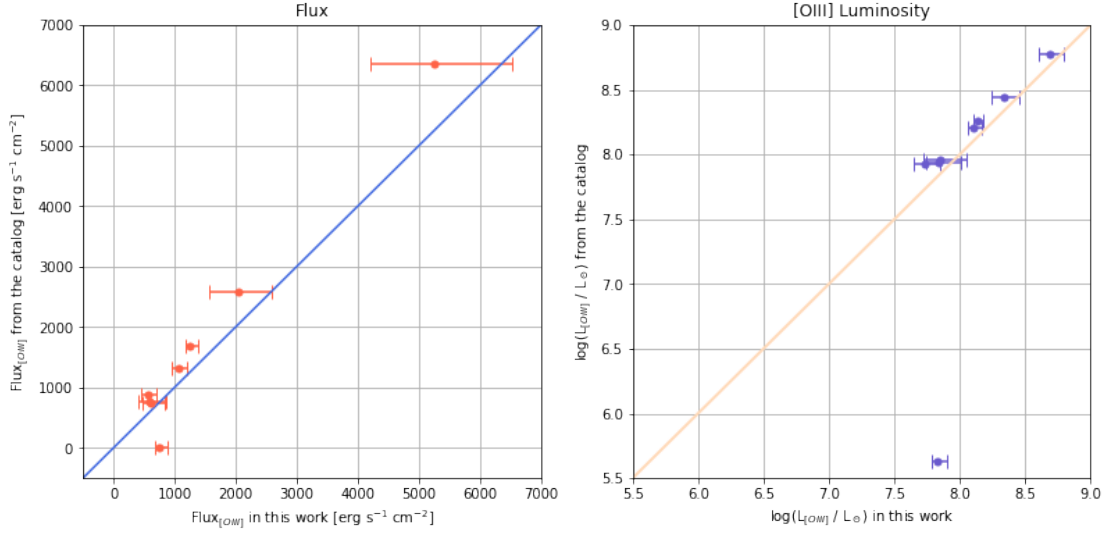


Figure 5.1: [OIII] flux calculated in this work versus [OIII] flux from the catalog (left). $\log\left(\frac{L_{\text{[OIII]}}}{L_{\odot}}\right)$ in this work against $\log\left(\frac{L_{\text{[OIII]}}}{L_{\odot}}\right)$ from the catalog (right).

and for $\text{H}\alpha$ velocity dispersion is

$$M_{\text{BH}} = (1.03 \times 10^6) M_{\odot} \left[\frac{\sigma_{*}}{200 \text{ km s}^{-1}} \right]^{0.44} \quad (5.3)$$

The stellar velocity dispersion of the object with MaNGA ID 1-43214 given in the catalog was reported as an error so it was not plotted here.

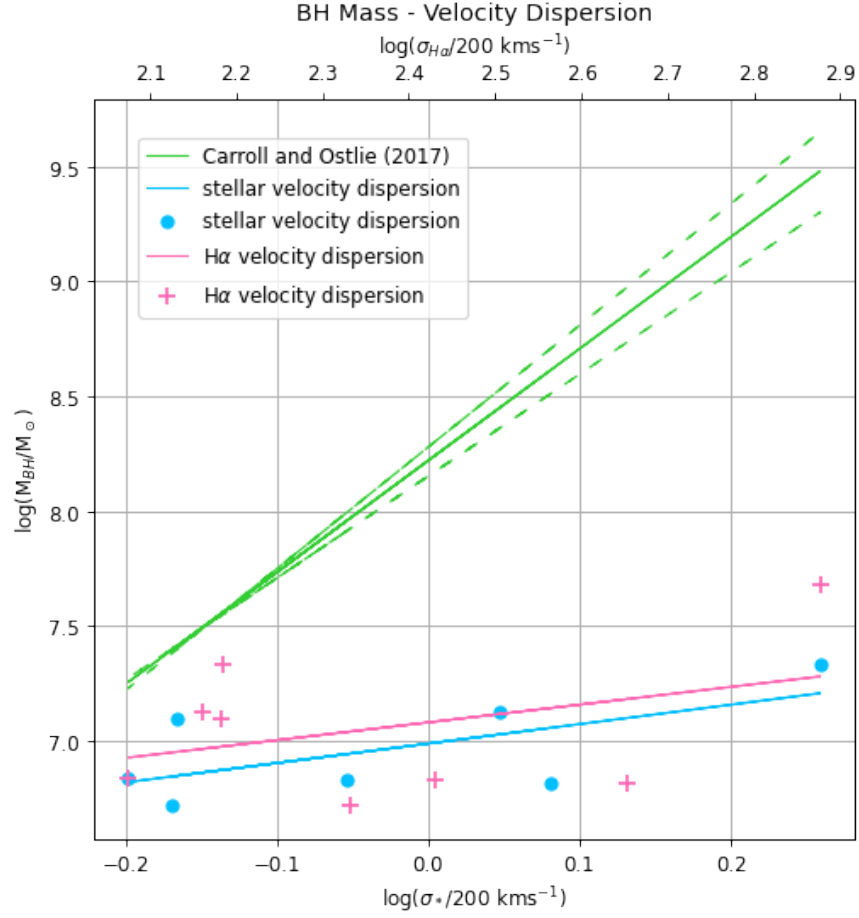


Figure 5.2: Correlation between $\log\left(\frac{\sigma_*}{200 \text{ km s}^{-1}}\right)$ and $\log\left(\frac{\sigma_{\text{H}\alpha}}{200 \text{ km s}^{-1}}\right)$ against $\log\left(\frac{M_{\text{BH}}}{M_{\odot}}\right)$, where blue data points and trend line shows the results of σ_* and the pink data points and trend line shows the data of $\sigma_{\text{H}\alpha}$. The green line displays the $M_{\text{BH}} - \sigma$ relationship, along with the upper bound and lower bound given in dashed lines, taken from Carroll and Ostlie (2017)

Table 5.1: Results of the calculated values, arranged in an increasing order of redshift.

| MaNGA ID | z | Flux _[OIII] [10^{-17} erg s $^{-1}$ cm $^{-2}$] | D _L [Mpc] | $\log\left(\frac{L_{\text{[OIII]}}}{L_{\odot}}\right)$ | $\log\left(\frac{M_{\text{BH}}}{M_{\odot}}\right)$ |
|----------|--------|--|----------------------|--|--|
| 1-156039 | 0.1147 | $758.1694^{+127.3393}_{-68.0173}$ | 533.1 | $7.8263^{+0.0674}_{-0.0408}$ | $6.8156^{+0.0674}_{-0.0408}$ |
| 1-43214 | 0.1180 | $5244.0399^{+1283.1545}_{-1032.1355}$ | 549.6 | $8.6927^{+0.0951}_{-0.0952}$ | $7.6819^{+0.0951}_{-0.0952}$ |
| 1-22948 | 0.1194 | $557.2729^{+156.4767}_{-109.9626}$ | 556.7 | $7.7302^{+0.1075}_{-0.0955}$ | $6.7195^{+0.1075}_{-0.0955}$ |
| 1-258599 | 0.1256 | $2044.0660^{+548.5921}_{-466.9476}$ | 587.9 | $8.3420^{+0.1033}_{-0.1126}$ | $7.3313^{+0.1033}_{-0.1126}$ |
| 1-72322 | 0.1262 | $1255.5285^{+123.8513}_{-76.4875}$ | 590.8 | $8.1346^{+0.0409}_{-0.0273}$ | $7.1239^{+0.0409}_{-0.0273}$ |
| 1-284293 | 0.1291 | $603.9552^{+238.6935}_{-127.8941}$ | 605.6 | $7.8383^{+0.1446}_{-0.1033}$ | $6.8276^{+0.1446}_{-0.1033}$ |
| 1-269632 | 0.1315 | $596.4699^{+270.0964}_{-177.3099}$ | 617.7 | $7.8500^{+0.1622}_{-0.1532}$ | $6.8393^{+0.1622}_{-0.1532}$ |
| 1-574402 | 0.1320 | $1068.8634^{+145.9220}_{-111.4273}$ | 620.5 | $8.1073^{+0.0556}_{-0.0478}$ | $7.0966^{+0.0556}_{-0.0478}$ |

CHAPTER 6

DISCUSSION

In figure 5.1, comparing the [OIII] flux and [OIII] luminosity calculated here against the values given in the catalog shows that the two sets of values are in an agreement, despite some outliers.

Also in figure 5.1, both left and right, the outlying data point which is lower than the others belongs to the object with the MaNGA ID 1-156039. From the spectrum, this object shows a peak at $\lambda = (1 + z) \times 5007$, but the shape of the peak, which is broken into two relatively close peaks with a heavy drop in the center, suggests that there could be an error. The fault could arise either because the peak shown in the spectrum is due to noise rather than the [OIII] emission, or that there is a mistake in the spectrum and instead of obtaining one complete peak, it is broken into two with a dip which causes the values calculated to be underestimated.

From figure 5.2, it can be seen that the result in this work greatly differs from the relationship reported by other works, but it is consistent amongst itself. The correlation between stellar and $H\alpha$ velocity dispersion against M_{BH} in this report is shown to be quite similar, with the exception that the values for $H\alpha$ velocity dispersion tend to be higher in general.

However, the relationship found in this work is very dissimilar to the that of the other literatures. Generally, previous works acquired the correlation to be as that in the equation 2.3, where the gradient of the trend line is about 3.75 to 5.57, and the y-intercept is approximately between 8.08 to 8.33. On the other hand, the gradient and the y-intercept of the trend line for the stellar velocity dispersion in this report is 0.85 and 6.99, and those of the $H\alpha$ velocity dispersion is 0.44 and 6.01, respectively, which is clearly seen that it is much lower than the reported values in other studies.

Further research could be made to look into the reason behind the inaccuracy of the results, and with that identified, black hole mass of objects in this work and beyond this work can be calculated more accurately, and a more precise $M_{\text{BH}} - \sigma$ can be shown.

CHAPTER 7

CONCLUSION

In this work, 8 objects at $z > 0.112$ has been chosen from SDSS - IV MaNGA DR 16 and their M_{BH} are calculated using the luminosity of [OIII] emission line. The flux, computed from the [OIII] emission line, have the values in between $557.27 \text{ erg s}^{-1} \text{ cm}^{-2}$, which belongs to the object with the MaNGA ID 1-22948, and $5244.04 \text{ erg s}^{-1} \text{ cm}^{-2}$, which is of the object with the MaNGA ID 1-43214.

The values of $\log \left(\frac{L_{[\text{OIII}]}}{L_{\odot}} \right)$ obtained are in the range 7.73 to 8.69, where, again, the lower value belongs to the object with the ID 1-22948, and the higher value belongs to the object with the ID 1-43214.

Similarly, the lowest value of $\log \left(\frac{M_{\text{BH}}}{M_{\odot}} \right)$, which is 6.72, belongs to the object with the MaNGA ID 1-22948, and the highest value, which is 7.68, is of the object with the MaNGA ID 1-43214.

Moreover, this report attempted to show the relationship between M_{BH} and σ , and to compare it with previous studies. It is found that there is a correlation between the two as suggested in other literatures, but the results obtained in this report is profoundly underestimated.

REFERENCES

- [1] Bundy, K., Bershadsky, M. A., Law, D. R., Yan, R., Drory, N., MacDonald, N., Wake, D. A., Cherinka, B., Sánchez-Gallego, J. R., Weijmans, A.-M., Thomas, D., Tremonti, C., Masters, K., Coccato, L., Diamond-Stanic, A. M., Aragón-Salamanca, A., Avila-Reese, V., Badenes, C., Falcón-Barroso, J., ... Zhang, K. (2014). Overview of the SDSS-IV MaNGA Survey : Mapping Nearby Galaxies at Apache Point Observatory. *The Astrophysical Journal*, 798(1), 7. <http://dx.doi.org/10.1088/0004-637X/798/1/7>
- [2] Carroll, B. W., & Ostlie, D. A. (2017). *An Introduction to Modern Astrophysics* (2nd ed.). Cambridge University Press.
- [3] Ferrarese, L. & Merritt, D. (2000). A Fundamental Relation Between Supermassive Black Holes and Their Host Galaxies. *The Astrophysical Journal*, 539(1), L9-L12. <https://doi.org/10.1086/312838>
- [4] Ferris, E. R., Blain, A. W., Assef, R. J., Hatch, N. A., Kimball, A., Kim, M., Sajina, A., Silva, A., Stern, D., Diaz-Santos, T., Tsai, C.-W., & Wylezalek, D. (2021). The black hole masses of extremely luminous radio-WISE selected galaxies. *Monthly Notices of the Royal Astronomical Society*, 502(1), 1527-1548. <https://doi.org/10.1093/mnras/stab048>
- [5] Frolov, V. P., & Zelnikov, A. (2011). *Introduction to Black Hole Physics* (1st ed.). Oxford University Press.
- [6] Gebhardt, K., Bender, R., Bower, G., Dressler, A., Faber, S. M., Filipenko, A. V., Green, R., Grillmair, C., Ho, L. C., Kormendy, J., Lauer, T. R., Magorrian, J., Pinkney, J., Richstone, D., & Tremaine, S. (2000). A Relationship between Nuclear Black Hole Mass and Galaxy Velocity Dispersion. *The Astrophysical Journal*, 539(1), L13-L16. <http://dx.doi.org/10.1086/312840>
- [7] Heckman, T. M. & Best, P. N. (2014). The Coevolution of Galaxies and Supermassive Black Holes: Insights from Surveys of the Contemporary Universe. *Annual Review of Astronomy and Astrophysics*, 52(1), 589-660. <http://dx.doi.org/10.1146/annurev-astro-081913-035722>
- [8] Law, D. R., Cherinka, B., Yan, R., Andrews, B. H., Bershadsky, M. A., Bizyaev, D., Blanc, G. A., Blanton, M. R., Bolton, A. S., Brownstein, J. R., Bundy, K.,

- Chen, Y., Drory, N., D'Souza, R., Fu, H., Jones, A., Kauffmann, G., MacDonald, N., Masters, K. L., ... Zhang, K. (2016). The Data Reduction Pipeline for the SDSS-IV MaNGA IFU Galaxy Survey. *The Astronomical Journal*, 152(4), 83. <http://dx.doi.org/10.3847/0004-6256/152/4/83>
- [9] Mo, H., van den Bosch, F., & White, S. (2010). *Galaxy Formation and Evolution* (1st ed.). Cambridge University Press.
- [10] McConnell, N. J., & Ma, C.-P. (2013). Revisiting the Scaling Relations of Black Hole Masses and Host Galaxy Properties. *The Astrophysical Journal*, 764(2), 184. <http://dx.doi.org/10.1088/0004-637X/764/2/184>
- [11] Nelson, C. H., Green, R. F., Bower, G., Gebhardt, K. & Weistrop, D. (2004). The Relationship Between Black Hole Mass and Velocity Dispersion in Seyfert 1 Galaxies. *The Astrophysical Journal*, 615(2), 652-661. <http://dx.doi.org/10.1086/424657>
- [12] Peterson, B. M. (1993). Reverberation Mapping of Active Galactic Nuclei. *Publications of the Astronomical Society of the Pacific*, 105(685), 247-268. <https://doi.org/10.1086/133140>
- [13] Romero, G. E., & Vila, G. S. (2014). *Introduction to Black Hole Astrophysics* (1st ed.). Springer.
- [14] Schneider, P. (2014). *Extragalactic Astronomy and Cosmology: An Introduction* (2nd ed.). Springer.
- [15] Shen, Y., Richards, G. T., Strauss, M. A., Hall, P. B., Schneider, D. P., Snedden, S., Bizyaev, D., Brewington, H., Malanushenko, V., Malanushenko, E., Oravetz, D., Pan, K., Simmons, A. (2011). A Catalog of Quasar Properties From SDSS DR7. *The Astrophysical Journal Supplement Series*, 194(2), 45. <https://doi.org/10.1088/0067-0049/194/2/45>
- [16] Sparke, L. S. & Gallagher, J. S., III. (2007). *Galaxies in the Universe : An Introduction* (2nd ed.). Cambridge University Press.
- [17] Wright, E. L. (2006). A Cosmology Calculator for the World Wide Web. *The Publications of the Astronomical Society of the Pacific*, 118(850), 1711-1715. <https://doi.org/10.1086/510102>
- [18] Wylezalek, D., Flores, A. M., Zakamska, N. L., Green, J. E., & Riffel, R. A. (2020). Ionized gas outflow signatures in SDSS-IV MaNGA active galactic nuclei. *Monthly Notices of the Royal Astronomical Society*, 492(4), 4680-4696. <https://doi.org/10.1093/mnras/staa062>

BIOGRAPHY

| | |
|------------------------------|---|
| NAME | Natacha Upra |
| DATE OF BIRTH | 4th April 1999 |
| PLACE OF BIRTH | Chiang Rai, Thailand |
| INSTITUTIONS ATTENDED | International Pioneers School, 2014 - 2017 Upper Secondary School (Grade 12) Mahidol University, 2017 - 2022 Bachelor of Science (Physics) |
| HOME ADDRESS | 415 m.5, Phaholyothin Rd, Rimkok, Muang Chiang Rai, Thailand, 57100 |
| E-MAIL | natachaupra@gmail.com |